

# Interplay of fast and slow dynamics in rare transition pathways: The disk-to-slab transition in the 2d Ising model

Clemens Moritz, Andreas Tröster, and Christoph Dellago

Citation: *The Journal of Chemical Physics* **147**, 152714 (2017);

View online: <https://doi.org/10.1063/1.4997479>

View Table of Contents: <http://aip.scitation.org/toc/jcp/147/15>

Published by the [American Institute of Physics](#)

---

## Articles you may be interested in

[Rock climbing: A local-global algorithm to compute minimum energy and minimum free energy pathways](#)  
*The Journal of Chemical Physics* **147**, 152718 (2017); 10.1063/1.4986298

[Predicting reaction coordinates in energy landscapes with diffusion anisotropy](#)  
*The Journal of Chemical Physics* **147**, 152701 (2017); 10.1063/1.4983727

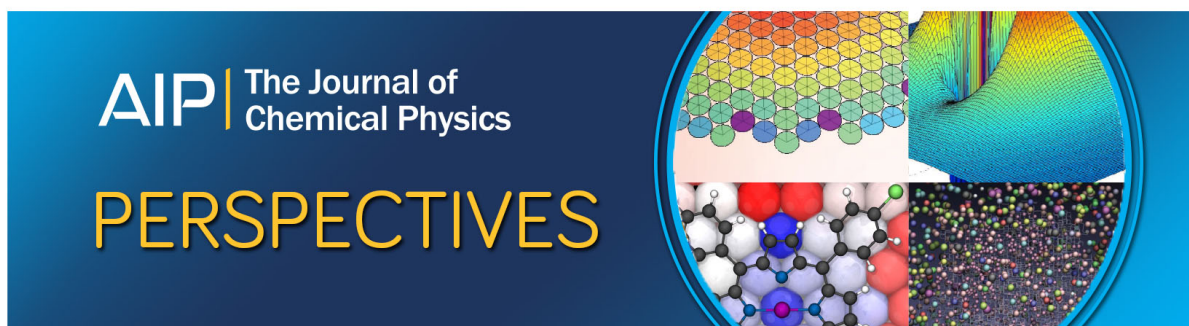
[Transition path sampling of rare events by shooting from the top](#)  
*The Journal of Chemical Physics* **147**, 152716 (2017); 10.1063/1.4997378

[Ab initio sampling of transition paths by conditioned Langevin dynamics](#)  
*The Journal of Chemical Physics* **147**, 152703 (2017); 10.1063/1.4985651

[Transition path times reveal memory effects and anomalous diffusion in the dynamics of protein folding](#)  
*The Journal of Chemical Physics* **147**, 152707 (2017); 10.1063/1.4993228

[A new class of enhanced kinetic sampling methods for building Markov state models](#)  
*The Journal of Chemical Physics* **147**, 152702 (2017); 10.1063/1.4984932

---



# Interplay of fast and slow dynamics in rare transition pathways: The disk-to-slab transition in the 2d Ising model

Clemens Moritz,<sup>1</sup> Andreas Tröster,<sup>2</sup> and Christoph Dellago<sup>1,a)</sup>

<sup>1</sup>*Faculty of Physics, University of Vienna, Boltzmannngasse 5, 1090 Vienna, Austria*

<sup>2</sup>*Institute of Materials Chemistry, Vienna University of Technology, Getreidemarkt 9, 1060 Vienna, Austria*

(Received 15 May 2017; accepted 24 July 2017; published online 9 August 2017)

Rare transitions between long-lived stable states are often analyzed in terms of free energy landscapes computed as functions of a few collective variables. Here, using transitions between geometric phases as example, we demonstrate that the effective dynamics of a system along these variables are an essential ingredient in the description of rare events and that the static perspective provided by the free energy alone may be misleading. In particular, we investigate the disk-to-slab transition in the two-dimensional Ising model starting with a calculation of a two-dimensional free energy landscape and the distribution of committor probabilities. While at first sight it appears that the committor is incompatible with the free energy, they can be reconciled with each other using a two-dimensional Smoluchowski equation that combines the free energy landscape with state dependent diffusion coefficients. These results illustrate that dynamical information is not only required to calculate rate constants but that neglecting dynamics may also lead to an inaccurate understanding of the mechanism of a given process. *Published by AIP Publishing.* [<http://dx.doi.org/10.1063/1.4997479>]

## I. INTRODUCTION

Free energy landscapes are a ubiquitous tool in the study of rare events—such as nucleation events in phase transitions or conformational changes in biomolecules—as they are often used to get a first sense of which regions in configuration space are relevant for a given process. Calculating such a landscape requires the choice of a small number of order parameters that are supposed to capture the important degrees of freedom of the process in question. Examples of such order parameters include the potential energy, the size of the largest cluster in the system (in the case of nucleation), or quantities like the number of native contacts, radii of gyration or root-mean-square deviations from the target structure (in biological systems).

However, care has to be taken in the interpretation of such free energy landscapes, since the choice of coordinates is not unique, even if the relevant degrees of freedom are captured. In particular, any non-linear transformation of the coordinates will change the free energy landscape, including features like the existence and height of free energy barriers.<sup>1</sup> Due to this arbitrariness, additional information on the dynamics along a chosen order parameter is required in order to reliably interpret a free energy landscape.<sup>2–6</sup>

With higher-dimensional free energy landscapes, additional complications arise, especially, if there is no clear physical relationship between the different order parameters used, as is often the case. For instance, one may be tempted to associate the gradient in such a landscape with a probability flux. However, flow directions,<sup>7–10</sup> the channels in which the transition proceeds,<sup>11–14</sup> and isocommittor lines<sup>15,16</sup> are determined

both by the free energy landscape and the dynamics of the system along the different order parameters and may deviate significantly from naive expectations. In particular, the combination of a fast and a slow degree of freedom that we will encounter in this work has been discussed using a toy model by Metzner, Schütte, and Vanden-Eijnden.<sup>17</sup>

Often, especially in the context of rate calculations, one would like to project the system onto a single variable, called a reaction coordinate, that is not only capable of distinguishing between reactant and product state but also describes the progress of the transformation in between. Due to the effects mentioned above, the free energy landscape may mislead us into a suboptimal choice for this reaction coordinate, which in turn negatively impacts the efficiency and accuracy of common rate calculation methods.

In the following, we use a simple model process to demonstrate some of the issues mentioned above: the disk-to-slab phase transition in the two-dimensional Ising model. Disk and slab phases are so called geometric phases,<sup>18</sup> which arise due to periodic boundary conditions used in simulations. They are characterized by different cluster shapes—spherical, cylindrical, and slablike in three dimensions—where the stability of the non-spherical shapes is due to the reduction of surface free energy that can be achieved by connecting a cluster to its periodic images. In two dimensions the number of geometries reduces to two: a disk phase and a slab phase.

The disk-to-slab transition is an example of a transition between different cluster (or bubble) geometries that play a role in different physical situations,<sup>19–24</sup> including the dewetting transition observed in volumes that are confined between hydrophobic surfaces.<sup>25–31</sup>

The mechanism of this dewetting has recently been discussed in detail by Remsing *et al.*,<sup>32</sup> who showed that it may involve the formation of a vapor bubble on one of the

<sup>a)</sup>christoph.dellago@univie.ac.at

surfaces that subsequently changes its shape to a vapor tube that connects the plates. Under some conditions, this mechanism reduces the free energy barrier that has to be overcome, by, in essence, circumventing the states that involve a vapor tube size that is close to critical. The disk-to-slab phase transition can be seen as a simplified version of this process.

Another interesting parallel can be drawn between the cylinder to sphere transition and the Rayleigh-Plateau instability.<sup>33–35</sup> As shown originally by Plateau,<sup>33</sup> a cylinder stabilized by surface tension is unstable against axial surface deformations with a wavelength larger than its circumference. Given a fixed box size, this sets a minimum radius a cylinder must have to be stable. However, in two dimensions, this (purely geometric) effect does not exist since a deformation of a 2d slab always leads to a larger surface and hence to a barrier opposing the decay of the slab.

In simulations of the Ising model, geometric phases have played a role in various cases. In particular, they can be used to calculate surface tensions,<sup>36,37</sup> and geometric phase transitions have been observed to hamper the sampling of free energy landscapes.<sup>38,39</sup> Furthermore, in an application of the string method,<sup>13,40</sup> geometric phase transitions have been discussed<sup>41</sup> as being part of the transition from the spin-down to the spin-up phase. Depending on the value of the external field, two transition mechanisms are possible. For strong fields, the critical configurations contain a disk shaped cluster. For weak fields, however, the disk-to-slab transition becomes the bottleneck. In this work we focus on the details of this disk-to-slab transition under conditions where the overall magnetization is fixed.

The remainder of this paper is structured as follows: Sec. II specifies the model that is investigated and introduces two order parameters that are then used to investigate the transition. In Sec. III we discuss the free energy landscape and the distribution of committor probabilities as well as the apparent disconnect between the two. Section IV explains how diffusion coefficients can be calculated reliably in this system, which is then used, in Sec. V, to build a two-dimensional model of the system that predicts the distribution of committor probabilities. In Sec. VI we recapitulate our findings and discuss some of their implications.

## II. MODEL AND ORDER PARAMETERS

We investigate the disk-to-slab phase transition in the two-dimensional Ising model with ferromagnetic nearest-neighbor interactions on a square lattice of size  $N = 100 \times 100$  and a vanishing magnetic field. The Hamiltonian is given by

$$\mathcal{H} = \sum_{\langle ij, i'j' \rangle} \sigma_{ij} \sigma_{i'j'}, \quad (1)$$

where the sum extends over all nearest-neighbor pairs and we have set the coupling constant to 1. The spins, denoted by  $\sigma_{ij}$  with  $i$  being the position in the  $x$ -direction and  $j$  the position in the  $y$ -direction, can take on values of +1 (up) and -1 (down) and the magnetization per spin of the system is given by  $m = (\sum_{i,j} \sigma_{ij})/N$ . Periodic boundary conditions apply in all directions. Since under these conditions the model is

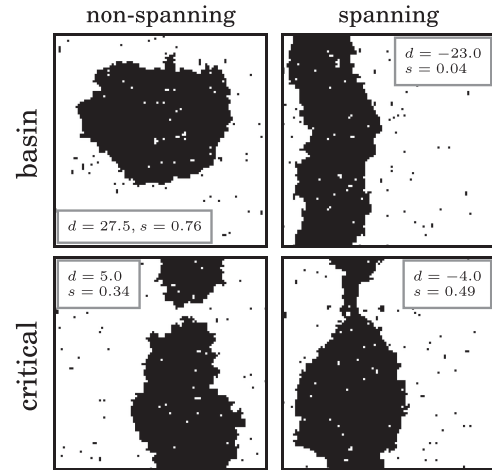


FIG. 1. Example configurations taken from simulations of the ferromagnetic Ising model at fixed magnetization of  $m = 0.36$  and temperature  $T = 0.7 T_c$ . The configurations in the top row are taken from the stable basin of the disk state and the slab state, respectively. The ones in the bottom row are critical configurations in the sense that their committor probabilities are close to 1/2.  $d$  and  $s$  are order parameters discussed in Sec. II.

symmetric with respect to a flip of all spins, we restrict the discussion to positive  $m$ .

In this case, given a fixed temperature  $T$  below the critical temperature  $T_c$ , three distinct phases can be found in order of descending magnetization: a homogeneous phase without a single dominant cluster of down spins, a disk phase where the bulk of the spins pointing down are in a single disk-shaped (*non-spanning*) cluster and a slab phase where this cluster is in contact with its own periodic copies (*spanning*). See Fig. 1 for examples of disk- and slab-shaped clusters.

In this study, the dynamics of the system are given by a Metropolis Monte Carlo procedure with moves that keep the magnetization constant by only exchanging spin positions. We distinguish between local<sup>42</sup> dynamics where only exchanges of neighboring spins are allowed and non-local dynamics that allow arbitrary exchanges. Local dynamics, which mimic mass transport in a more realistic system, are used in all simulations where dynamic properties are probed, while non-local moves are used for free energy calculations to enhance sampling. The unit of time  $t$  is a Monte Carlo sweep, i.e.,  $N$  attempted single spin-exchange moves.

In the following discussion the reduced temperature is set to  $\theta = T/T_c = 0.7$  and the magnetization to  $m = 0.36$ , where the slab state is metastable with respect to the disk state.

We will now introduce the order parameters  $d$  and  $s$  that we will use to describe transitions between the disk state and the slab state. For reference, Fig. 1 shows examples of configurations together with their respective  $d$ - and  $s$ -values.

### A. The minimum distance/width order parameter $d$

We first introduce an order parameter that is capable of distinguishing between disk- and slab-shaped clusters as well as between intermediate shapes. To do so, we identify the largest (geometric<sup>43,44</sup>) cluster of spins, i.e., the largest connected cluster of spins that are neighbors of each other and point down. If this cluster is a non-spanning cluster, we characterize its shape by finding the shortest distance,  $d_{\text{image}}$ , between the

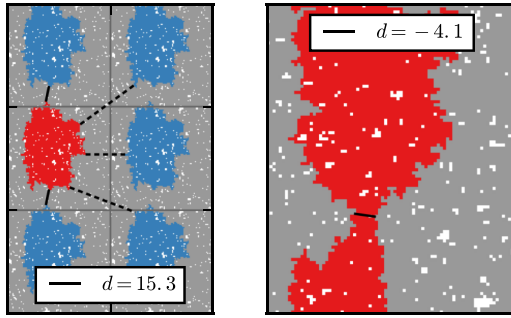


FIG. 2. Examples of the construction of the minimum distance/width order parameter  $d$  for non-spanning clusters (left) and spanning clusters (right). The cluster indicated in red is the largest cluster of spins pointing down, and the one in gray is the largest cluster pointing in the up direction. White spins do not belong to either of these clusters and the blue clusters are periodic copies of the red cluster. On the left, the smallest distance between the largest cluster and its periodic images is used as an order parameter while on the right the smallest distance between the two surfaces of the oppositely oriented cluster is measured. The latter is a proxy for the smallest width found along the length of the red cluster.

surface of the cluster and the surfaces of any of its periodic images (see Fig. 2). If the cluster is a spanning one, we instead characterize constrictions along its length by finding the smallest distance between the surfaces of the delimiting cluster of up spins, which is shown in gray on the right side of Fig. 2. This quantity is denoted by  $d_{\text{width}}$ .

The combined minimum distance/width coordinate  $d$  is then given by

$$d = \begin{cases} d_{\text{image}} & \text{for non-spanning clusters} \\ -d_{\text{width}} + 3 & \text{for spanning clusters} \end{cases}, \quad (2)$$

where the number 3 is added to  $-d_{\text{width}}$  in order to close a gap in the possible values of  $d$  that is due to the lowest possible  $d_{\text{image}}$  and  $d_{\text{width}}$  being  $\sqrt{2}$  (when the closest spins of the two clusters are offset by one diagonal step) and 2 (when there is a bridge of exactly one spin left), respectively. Consequently, for spanning clusters,  $d$  is less than or equal to 1, and, for non-spanning clusters,  $d$  is larger than 1. Furthermore, the order parameter  $d$  differentiates between different cluster shapes both for spanning and non-spanning clusters and yields information on the local structure of the cluster around the connecting bridge to its periodic images.

The distance order parameter  $d$  has units of one lattice constant.

## B. The shape order parameter $s$

As we will see later, in order to arrive at a complete picture of the dynamics of the transition, a second order parameter that characterizes the overall shape of the cluster is required. A straightforward way to do that for non-spanning clusters would be to use the ratio of the main moments of inertia of the cluster. However, this method breaks down as soon as the cluster is a spanning cluster since the main moments of inertia are no longer well defined.

Instead, we will use a proxy in Fourier space, where, for a system with  $n \times n$  spins, we first take a Fourier transform of

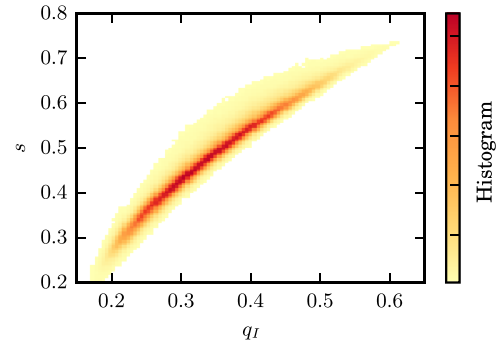


FIG. 3. Histogram of  $qI$ - $s$  value pairs calculated from configurations that contain non-spanning clusters found in trajectories obtained from transition path sampling simulations<sup>45</sup> of the disk-to-slab transition.  $qI$  is defined as the ratio of the smaller main moment of inertia of the cluster to the larger one. The  $s$  values are highly correlated to the  $qI$  values indicating that they are an equally good measure for how disk-like a cluster's shape is.

the configuration yielding the components

$$\tilde{\sigma}_{jk} = \frac{1}{n^2} \sum_{l,m=1}^n \sigma_{lm} \exp \left[ \frac{2\pi i}{n} (jl + km) \right] \quad (3)$$

and then take the (dimensionless) ratio

$$s = \min \left( \frac{|\tilde{\sigma}_{01}|}{|\tilde{\sigma}_{10}|}, \frac{|\tilde{\sigma}_{10}|}{|\tilde{\sigma}_{01}|} \right). \quad (4)$$

Here,  $\tilde{\sigma}_{10}$  and  $\tilde{\sigma}_{01}$  are the longest wavelength components in the  $x$  and  $y$  directions, respectively.

The order parameter  $s$  takes on values from close to 0—indicating configurations that are asymmetric with respect to an exchange of the  $x$  and  $y$  directions—to 1 indicating that the largest cluster in the system is close to being symmetric. Its values are highly correlated to the ratio of the main moments of inertia for non-spanning clusters (see Fig. 3), but it is also well defined for spanning clusters.

## III. FREE ENERGIES AND THE COMMITTOR

We start our investigation of the mechanism of the disk-to-slab phase transition by computing the free energy landscape  $\beta F(d, s) = -\log [P(d, s)]$ , where  $P(d, s)$  is the equilibrium probability density as a function of  $d$  and  $s$ ,  $\beta = 1/k_{\text{B}}T$ , and  $k_{\text{B}}$  is Boltzmann's constant. We do so by performing umbrella sampling simulations in the plane spanned by the  $d$  and  $s$  coordinates. Configurations are biased using a series of harmonic bias potentials that are centered at different points in the  $d$ - $s$  plane. The resulting probability distributions are then reweighted using the weighted histogram analysis method (WHAM).<sup>46,47</sup> Figure 4 shows the result of these calculations. The slab state,  $\mathcal{A}$ , is metastable with respect to the disk state,  $\mathcal{B}$ , by  $6.4 k_{\text{B}}T$  and the two states are separated by a barrier with a height of roughly  $8 k_{\text{B}}T$  measured from the minimum within state  $\mathcal{A}$ .

In order to assess the quality of the two chosen order parameters  $d$  and  $s$ , transition path sampling<sup>45</sup> (TPS) simulations using aimless shooting<sup>49</sup> and variable trajectory lengths have been used to obtain trajectories transitioning from state  $\mathcal{A}$  to state  $\mathcal{B}$ . Configurations are assumed to have reached the basins if the value of  $d$  is smaller than  $-15$  or greater than 26, respectively. The trajectories consist of segments with a

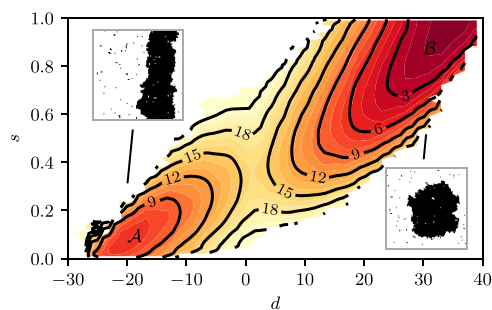


FIG. 4. Free energy  $F/k_B T$  (black isolines) of the 2D Ising model at magnetization per spin  $m = 0.36$  and reduced temperature  $\theta = 0.7$  as a function of the minimum distance/width order parameter  $d$  and the shape order parameter  $s$ . The insets show examples of a slab-shaped cluster (top left, basin  $A$ ) and a disk-shaped cluster (bottom right, basin  $B$ ). The zero-point of the free energy is chosen to coincide with the free energy minimum found in state  $B$ . The data were obtained by a series of umbrella sampling simulations with harmonic biases and subsequent reweighting using WHAM.<sup>46–48</sup>

length of 2000 MC sweeps each and the shooting point is randomly shifted forward or backward in time by 20 segments or the same shooting point as in the previous trajectory is chosen. Figure 5 shows example trajectories obtained from these simulations.

As was mentioned in the Introduction, a good reaction coordinate is able to characterize the progress of the transition. This means that solely based on this coordinate, one is able to predict the so-called committor probability. The committor probability,  $p_B$ , of a configuration is the probability of reaching state  $B$  before reaching state  $A$  averaged over trajectories started from the configuration. In our case, the averaging is done over trajectories computed with different random number generator seeds.

We computed committor values for configurations from pathways harvested in TPS runs. We estimated  $p_B$  by shooting trajectories from a given configuration and counting the number of times these trajectories reach state  $B$  first. The number

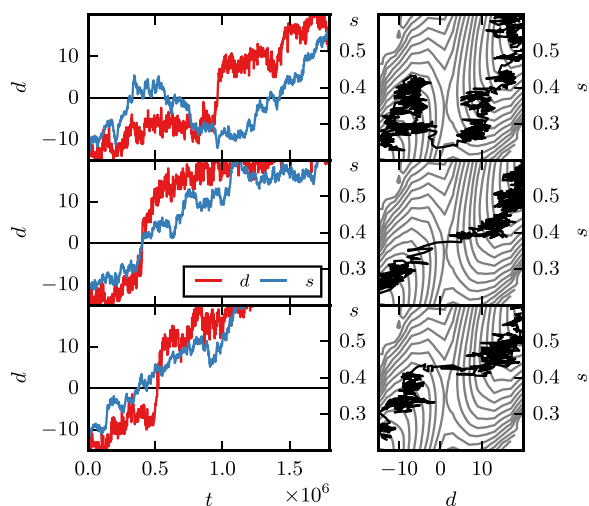


FIG. 5. Example trajectories of the disk-to-slab transition obtained from transition path sampling. The order parameters  $d$  and  $s$  are shown as a function of time (left) and as they appear projected onto the free energy landscape (right, isolines are placed  $1 k_B T$  apart). Time is given in units of Monte Carlo sweeps. Note that the transition over the ridge of the free energy landscape at  $d = 0$  progresses at a time scale that is much faster than the evolution of the  $s$  coordinate.

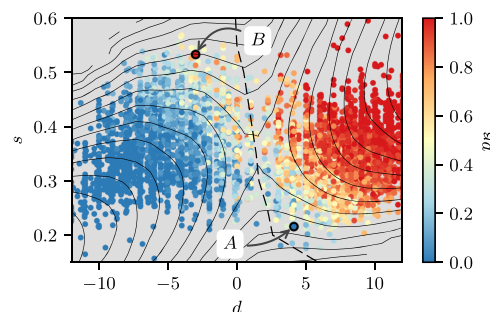


FIG. 6. Committor probabilities  $p_B$  calculated for a section of the free energy landscape in the  $d$ - $s$  plane shown in Fig. 4. The black lines are isolines of the free energy drawn in intervals of  $k_B T$ . The colored dots indicate the committor probabilities towards the disk state, and the dashed black line represents the ridge of the free energy landscape that separates the basins of attraction of the disk and the slab states. The configurations marked with  $A$  and  $B$  are shown in Fig. 7.

of shots was chosen such that the statistical uncertainty of the estimated probability is smaller than 10%.<sup>50</sup>

Figure 6 shows the resulting committor probabilities together with the free energy  $\beta F(d, s)$ . The shape of the free energy barrier suggests that the committor probability is determined by the value of the  $d$ -coordinate only. However, an examination of the committor probabilities calculated from simulation paints a different picture, in which there is a significant dependence of the committor on the value of the  $s$ -coordinate. In particular, some configurations that, based on the free energy landscape, seem to be in the basin of attraction of state  $A$  ( $B$ ) have a greater (smaller) than 1/2 chance to evolve into the disk state  $B$ . Such configurations, marked with  $A$  and  $B$ , are shown in Fig. 7.

At this point one may suspect that we have not yet captured all the relevant degrees of freedom that determine the progress of the transition. However, Fig. 8—which shows an optimized coordinate obtained using a likelihood maximization method due to Peters and Trout<sup>49</sup>—suggests that the committor can be fairly accurately described using only  $d$  and  $s$ . In the following we will reconcile this apparent disconnect by including the dynamics along  $d$  and  $s$  into our considerations.

We start by noting that in the trajectories shown in Fig. 5, the system spends a much larger amount of time close to the free energy barrier than it takes to cross the barrier to the other side. The  $s$ -coordinate evolves slowly because a large number of spins need to change collectively in order to change the shape parameter  $s$  appreciably. Hence, for the dynamics chosen for the system, changing  $s$  corresponds to the diffusive rearrangement of spins over long distances. In contrast, close

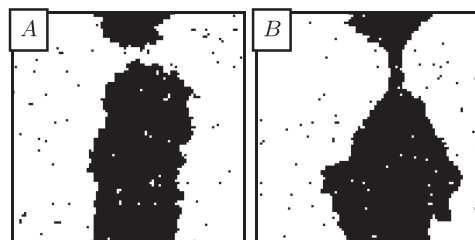


FIG. 7. Example configurations  $A$  and  $B$  marked in Fig. 6. These configurations are located at  $(d = 4.1, s = 0.216)$  and  $(d = -3.0, s = 0.532)$  and have committor probabilities towards the disk state of 0.362 and 0.958, respectively.

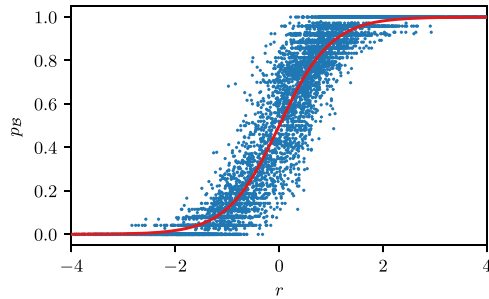


FIG. 8. Committor probabilities towards the disk state as a function of a combined reaction coordinate  $r = 0.18 d + 6.4 s - 2.6$ . The parameters have been determined using a likelihood maximization procedure.<sup>49</sup> The red line represents the committor model function used for the optimization.

to the barrier region, a change in the  $d$ -coordinate only requires the movement of relatively few spins and hence changes along the  $d$ -direction proceed much faster. As we will see later, this difference in relaxation times along the  $d$ - and  $s$ -direction strongly influence the distribution of committor probabilities. This dynamical behavior can be characterized using a coordinate dependent diffusion coefficient tensor<sup>13,17,51,52</sup>  $D_{ij}(d, s)$ , which we will calculate in Sec. IV.

#### IV. CHARACTERIZING SYSTEM DYNAMICS

In order to determine  $D_{ij}$ , we first employ the method of Im and Roux<sup>53,54</sup> to calculate mean square displacements (MSDs) along the two coordinate directions that are corrected (up to first order) for the drift of the order parameters that is due to the underlying free energy landscape. Starting from equilibrium configurations within narrow ranges of  $d$ - and  $s$ -values, we generate short, unbiased trajectories. Using the coordinate  $d$  as an example, the MSD is then estimated by

$$\langle \delta \tilde{d}^2 \rangle_t = \langle (\tilde{d}(t) - \langle \tilde{d} \rangle_t)^2 \rangle_t. \quad (5)$$

Here  $\tilde{d}(t) = d(t) - d(0)$  and the averages  $\langle \dots \rangle_t$  are taken over the trajectories at time  $t$  from their start. This procedure takes the mean drift (given by  $\langle \tilde{d} \rangle_t$ ), as well as the slightly different starting points of the trajectories into account.

Figure 9 shows the results of this calculation. In principle, linear fits to the data shown then yield the diffusion coefficients  $D_{XX}$ . While this is certainly true for the  $D_{ss}$  component, the MSDs along the  $d$ -direction are highly non-linear even for long times, making it impossible to reliably determine the value for  $D_{dd}$  this way.

Before we address this problem, note that Fig. 10 shows the correlations

$$C_{ds}(t) = \frac{\langle (\delta \tilde{d})(\delta \tilde{s}) \rangle_t}{\sqrt{\langle (\delta \tilde{d})^2 \rangle_t} \sqrt{\langle (\delta \tilde{s})^2 \rangle_t}}, \quad (6)$$

which are small and, hence, in the following we will treat the fluctuations in the  $d$ - and  $s$ -direction to be independent of each other by assuming  $D_{ij}$  to have the diagonal form

$$(D_{ij})(\vec{x}) = \begin{pmatrix} D_d(\vec{x}) & 0 \\ 0 & D_s(\vec{x}) \end{pmatrix}. \quad (7)$$

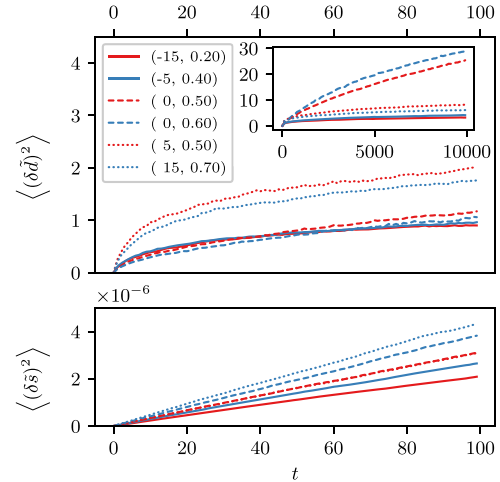


FIG. 9. Estimates for local mean square displacements measured using the method of Im and Roux.<sup>9,53,54</sup> Different lines correspond to different starting points of the trajectories, which are given in the legend as  $d$ - $s$  pairs. Notice the distinct non-linear behavior along the  $d$  direction (top), indicating the presence of strong memory effects at short time scales. The starting points at the top of the free energy barrier (dashed lines) show a markedly different behavior for long times (inset) due to the fact that two groups of trajectories separate—those developing towards the slab basin and those headed towards the disk basin.

The values for  $D_s$  obtained by fitting to the MSDs are shown in the lower panel of Fig. 12.

In order to obtain reliable results for  $D_d(\vec{x})$ , we use a Bayesian method introduced by Best and Hummer,<sup>5,55</sup> which is based on discretizing order parameter axes into bins followed by the maximization of the likelihood,

$$L = \prod_{\alpha} (e^{t_{\alpha} R})_{i_{\alpha} j_{\alpha}}. \quad (8)$$

Here,  $R$  is the matrix of transition rate constants between the bins,  $t_{\alpha}$  is the lag time between two measurements of the order parameter and the product runs over all transitions of the system observed in a set of trajectories. The components of  $R$  obey the conditions,

$$R_{ij} = \begin{cases} -\sum_{l \neq i} R_{il} & \text{if } i = j, \\ R_{ji} P_i / P_j & \text{if } i < j, \end{cases} \quad (9)$$

where  $P_i$  is the equilibrium probability of finding the system in bin  $i$ . Assuming that only the transition rates between neighboring bins are non-zero (i.e., we assume that the system transitioning from bin  $i$  to  $j$  has to pass through all bins in between) leaves us with  $\mathcal{N} - 1$  independent components,

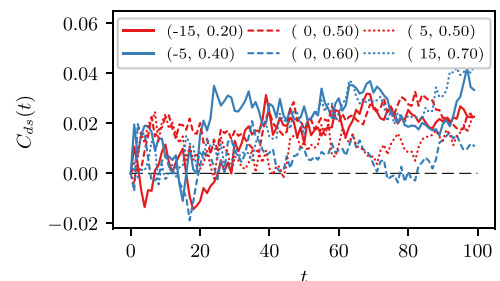


FIG. 10. Correlation  $C_{ds}$  of mean displacements given by Eq. (6). The displacements in the  $d$ - and  $s$ -direction are largely uncorrelated from each other.

where  $\mathcal{N}$  is the number of bins used. The diffusion coefficient between bin  $i$  and  $i + 1$  along a coordinate  $X$  with a bin width of  $\Delta X$  is then given by<sup>55,56</sup>

$$D_{i,i+1} = \Delta X^2 R_{i+1,i} \left( \frac{P_i}{P_{i+1}} \right)^{1/2}. \quad (10)$$

The advantage of this method is that we can choose a lag time  $\tau = t_\alpha$  that is long enough, such that the memory effects seen in the mean square displacements subside while we can still deal with the considerable drift that occurs within this lag time.

Since  $D_d$  is considered to be independent of the  $s$ -direction and the evolution along the  $s$ -direction is slow, we can perform this calculation independently in parallel slices along lines of constant  $s$ . These slices have a width of  $\Delta s = 0.025$  and each of these slices is split into bins of size  $\Delta d = 2$ . As suggested in Refs. 5 and 55, we count the number of transitions between these bins,  $N_{ij}$ , for a set of trajectories and subsequently vary the rate parameters  $R_{ij}$  in order to maximize the log-likelihood,

$$\log \tilde{L} = \sum_{ij} N_{ij} \log [\exp(\tau R)_{ij}] + \sum_i \frac{(D_{i+1,i} - D_{i,i-1})^2}{2\epsilon^2}, \quad (11)$$

where the second sum is a smoothing prior. We take the  $P_i$  from previous free energy calculations. The matrix exponential  $\exp(\tau R)$  is evaluated using a scaling-and-squaring method<sup>57</sup> as implemented in the python package SciPy.<sup>58</sup> The value of  $\epsilon$  was chosen to be  $3 \cdot 10^{-4}$ , which is on the order of the eventual values obtained for  $D_d$ , in order to smooth large statistical fluctuations.

The lag time is chosen by varying the lag time until one observes a plateau in the resulting diffusion coefficients. Figure 11 shows the results of such a calculation as a function of lag time for a single slice. At  $\tau = 30\,000$  the values of the diffusion coefficients seem to have reached a plateau while statistics are

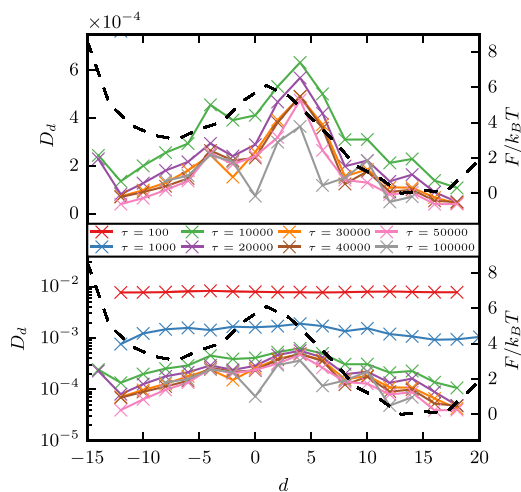


FIG. 11. Diffusion coefficient  $D_d$  measured using the likelihood maximization method as a function of the chosen lag time  $\tau$  for the  $s = 0.375\text{--}0.400$  slice, chosen here as an example. Both panels show the same data but the lower one uses a logarithmic y-axis. The dashed, black line indicates the free energy profile along the slice. Time is measured in units of Monte Carlo sweeps.

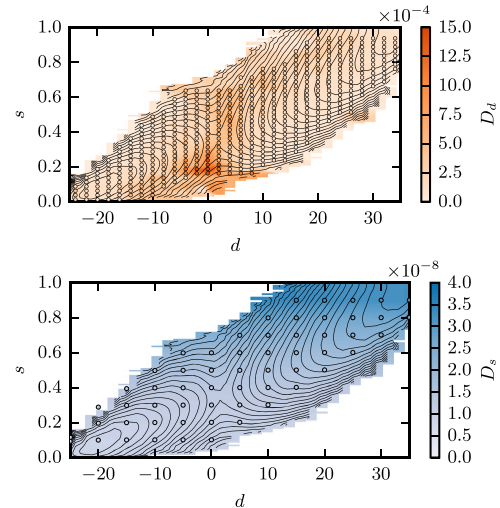


FIG. 12. Measured diffusion coefficients (circles) and cubic spline interpolation of these values (background) for the  $D_d$  component (top) and the  $D_s$  component (bottom). The diffusion coefficients are measured using a likelihood maximization method due to Hummer and co-workers<sup>5,55</sup> in the  $d$ -direction and the mean-square displacement based ansatz by Im and Roux<sup>9,53,54</sup> in the  $s$ -direction. The unit of time  $t$  is 1 Monte Carlo sweep and the black lines indicate the free energy landscape where the lines are separated by  $1 k_B T$ .

still reasonably good. This lag time is used to calculate the values of  $D_d$  shown in the upper panel of Fig. 12.

## V. UNDERSTANDING THE COMMITTOR

In this section we will demonstrate that the shape of the committor distribution can be largely explained on the basis of the order parameters we have already introduced,  $d$  and  $s$ , if one includes the dynamics of the system. Based on the free energy landscape and the diffusion coefficients we have obtained, we will first identify and estimate the time scales involved in the transition in order to gain an intuitive understanding, followed by an approach that uses a Smoluchowski equation to model the process.

### A. A qualitative explanation

We start by noting that the drift towards the stable basins along the  $s$ -direction is slow compared with the relaxation time along the  $d$ -direction. Hence, in the following calculation we assume that a local equilibrium along slices of constant  $s$  develops and consequently crossing the barrier becomes a one-dimensional problem associated with a time scale  $\tau_{\text{cross}}(s)$ , similar to a previous discussion of multicomponent nucleation by Trinkaus.<sup>7</sup>

We then compare  $\tau_{\text{cross}}$  to the time scale  $\tau_{\text{drift}}$  that is associated with the diffusion along the  $s$ -direction; if  $\tau_{\text{cross}} \gg \tau_{\text{drift}}$ , the system is likely to stay on the same side of the barrier, whereas if they are comparable, one expects to see a finite probability of crossing to the other side of the barrier.

Given the free energy landscape and the diffusion coefficient  $D_d(s)$ , we can estimate  $\tau_{\text{cross}}$  by the expression,

$$\tau_{\text{cross}} \sim \frac{[\Delta d(s)]^2}{D_d(s)} e^{\beta F^\ddagger(s)}, \quad (12)$$

where  $F^\ddagger(s)$  is the height of the free energy barrier found when one looks only at a slice of the free energy landscape along a

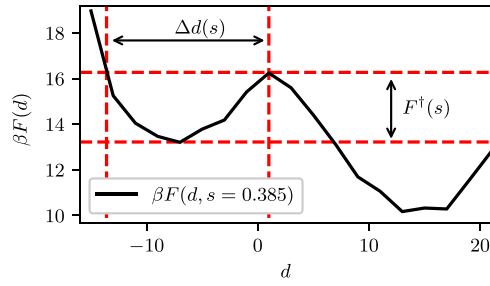


FIG. 13. Illustration of the quantities used to estimate the time scale of barrier crossing given by Eq. (12). The black line indicates the free energy  $\beta F(d)$  along a slice of constant  $s$ . The quantities shown are used to estimate the crossing time from the basin of attraction of slab states towards the disk states. The calculation for crossing from disk to slab proceeds analogously using the width and depth of the disk basin (located at  $d \approx 15$ ) instead.

line of constant  $s$  and  $\Delta d$  is a length scale given by the width of the basin as seen along the slice (see Fig. 13). Note the similarity of expression (12) to the Kramers<sup>59,60</sup> rate expression, where, in contrast, the length scales are provided by the curvatures of the free energy profile.<sup>61</sup>

$\tau_{\text{drift}}$  is related to the drift of the system along the  $s$ -axis. As the system moves towards the stable basin and the barrier height  $F^\ddagger$  becomes larger,  $\tau_{\text{cross}}$  grows exponentially as a function of  $F^\ddagger$ . This change in barrier height can be used to estimate the time it takes until the system has moved to an area within the free energy landscape, where the rate of transitions has considerably changed relative to where the system has started from. We define a characteristic length  $\Delta s$  as the distance at which the barrier height has increased by  $\Delta F^\ddagger = 1 k_B T$ ,

$$1 = \beta \Delta F^\ddagger(s) \approx \beta \frac{\partial F^\ddagger(s)}{\partial s} \Delta s. \quad (13)$$

In order to estimate  $\tau_{\text{drift}}$ , we look at the mean first passage time of trajectories started at  $s = s_0$  at a point  $s_0 - \Delta s$ , assuming that the free energy landscape has a constant slope. This time is given by (see the Appendix and Ref. 52)

$$\begin{aligned} \tau_{\text{drift}} &\sim \frac{\Delta s}{D_s \beta \left( \frac{\partial F(s)}{\partial s} \right)_{s=s_0}}, \\ &= \frac{1}{D_s \beta^2 \left( \frac{\partial F(s)}{\partial s} \right) \left( \frac{\partial F^\ddagger(s)}{\partial s} \right)}, \end{aligned} \quad (14)$$

where  $\beta F(s) = -\log [\int dd' \exp(-\beta F(d', s))]$  and the integration extends over the appropriate free energy basin.

The ratio of the two time scales, given by

$$\frac{\tau_{\text{cross}}}{\tau_{\text{drift}}} = \frac{D_s}{D_d} \beta^2 (\Delta d(s))^2 \left| \frac{\partial F(s)}{\partial s} \frac{\partial F^\ddagger(s)}{\partial s} \right| e^{\beta F^\ddagger(s)}, \quad (15)$$

is shown in Fig. 14.

One can see that in the outer regions with  $s \lesssim 0.25$  and  $s \gtrsim 0.45$  the crossing time becomes comparable to the drift time. Furthermore, if  $\tau_{\text{cross}}/\tau_{\text{drift}}$  is close to 1 in one direction of the transition, it is orders of magnitude larger in the reverse direction. This suggests that in these regions the probability of crossing from one side of the barrier to the other is non-zero and, on the other hand, after the barrier has been crossed, the probability of going back is small. Hence, we arrive at the explanation of why the committor probabilities in these regions take on the values shown in Fig. 5. It takes a long time to change

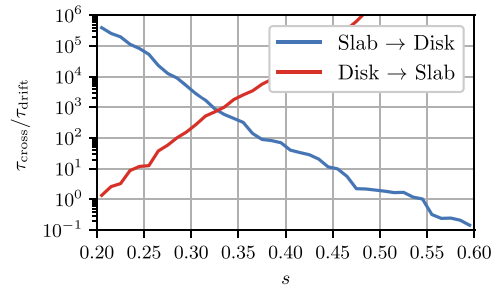


FIG. 14. Comparison of the time scales that are required to drift towards the stable basin,  $\tau_{\text{drift}}$ , and to cross the barrier to the other side of the transition,  $\tau_{\text{cross}}$ , if one assumes equilibrium along a slice of constant  $s$ . The results have been obtained by numerical evaluation of Eq. (15) using the free energy data shown in Fig. 4 and assuming  $D_s/D_d = 3.2 \cdot 10^{-5}$ , which is the value at the saddle point.

the overall shape of the cluster, and in this time, fluctuations can occur that make the system cross the barrier. However, once the barrier has been crossed, the probability of going back the other way is small because the global shape of the cluster disfavors such fluctuations. In other words, there is a high probability that the bridge of spins that can be seen in the right panel of Fig. 7 is severed before the cluster has changed its shape into a slab and, conversely, the likelihood of a bridge forming in the left panel before the cluster becomes disk-shaped is high.

## B. Smoluchowski analysis

A more accurate analysis of the system's behavior given the free energy landscape and the diffusion coefficients can be achieved by modeling the dynamics of the system using a two-dimensional Smoluchowski equation. A similar approach has previously been employed by Metzner, Schütte, and Vanden-Eijnden<sup>17</sup> in order to predict the behavior of a two-dimensional toy model. We use a generalized ansatz that takes into account state dependent diffusion coefficients.<sup>51,52</sup> In this case, the probability density  $\rho(\vec{x}, t)$  satisfies the equation,

$$\begin{aligned} \frac{\partial \rho}{\partial t} &= - \sum_{ij} \frac{\partial}{\partial x_i} \left[ \left( \frac{\partial D_{ij}}{\partial x_j} - \beta D_{ij} \frac{\partial F}{\partial x_j} \right) \rho \right] \\ &+ \sum_{ij} \frac{\partial^2}{\partial x_i \partial x_j} [D_{ij} \rho], \end{aligned} \quad (16)$$

where  $\vec{x} = (d, s)$ ,  $F = F(\vec{x})$  is the free energy shown before, and  $D_{ij}(\vec{x})$  are position dependent diffusion coefficients. This form of the Fokker-Planck equation<sup>62</sup> mimics a random walk on a potential of mean force given by the free energy  $F$  and, at the same time, guarantees that the steady state solution is given by the equilibrium distribution  $e^{-\beta F}$ .

In this model the committor  $p_B(\vec{x})$  is then determined by the corresponding backward (or adjoint) equation,<sup>17,52</sup>

$$\sum_{ij} \left( \frac{\partial D_{ij}}{\partial x_j} - \beta D_{ij} \frac{\partial F}{\partial x_j} \right) \frac{\partial p_B(\vec{x})}{\partial x_i} + \sum_{ij} D_{ij} \frac{\partial^2 p_B(\vec{x})}{\partial x_i \partial x_j} = 0. \quad (17)$$

The reflecting boundary condition

$$\sum_i n_i D_{ij} \frac{\partial p_B(\vec{x})}{\partial x_j} = 0, \quad (18)$$

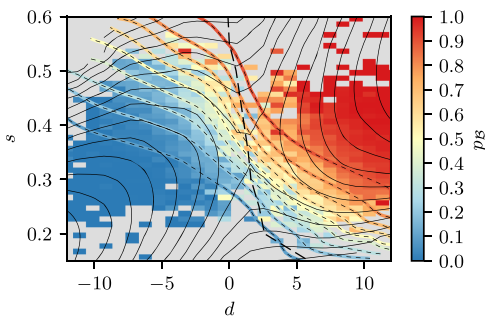


FIG. 15. Solution  $q(d, s)$  of the adjoint Smoluchowski equation (17) (isolines with black dashes) using the free energy data obtained from simulation of the disk-slab transition and the diffusion coefficients shown in Fig. 12. The background color shows committor values shown in Fig. 5 averaged over squares of size  $1.0[d] \times 0.01[s]$ , and the dashed black line represents the ridge of the free energy landscape that separates the basins of attraction of the disk and the slab state.

where  $\vec{n}$  is a normal vector on the domain and the boundary conditions that surround regions  $\mathcal{A}$  and  $\mathcal{B}$ ,

$$p_B(\vec{x})|_{\partial\mathcal{A}} = 0, p_B(\vec{x})|_{\partial\mathcal{B}} = 1, \quad (19)$$

close the set of equations.

This system of equations can be solved using a finite difference scheme similar to the one employed in Ref. 17 using the free energy and diffusion coefficients measured from simulation as input. The result of such a calculation is shown in Fig. 15. It recovers the basic features of the committor observed in the brute force simulations. In particular, the  $p_B = 1/2$  committor line significantly deviates from the ridge of the free energy landscape and the regions close to the barrier that have

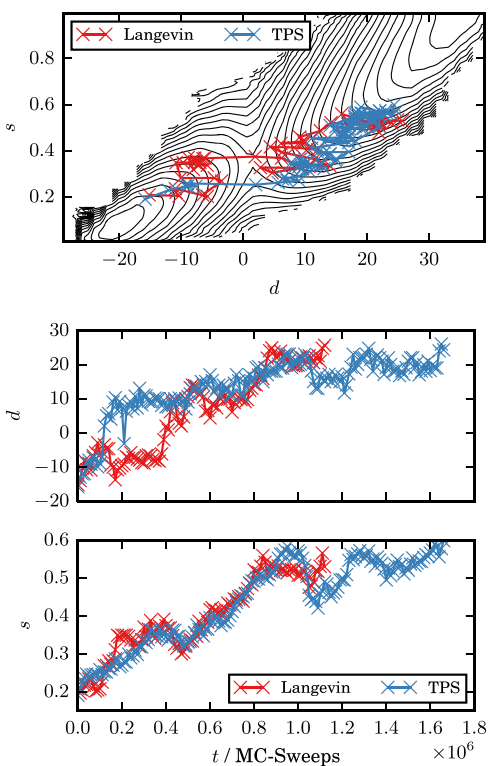


FIG. 16. Example trajectories obtained from TPS simulations (blue) and by integrating the Langevin equation (20) (red) from a state at the saddle point as they appear projected onto the  $d$ - $s$ -plane (top) and as a function of time (bottom).

large or small values of  $s$  have a significant probability of evolving to the other side of the free energy barrier.

We can also write down a corresponding Langevin equation, whose realizations will—if evaluated using Ito's interpretation (i.e., by evaluating the drift and diffusion terms at the beginning of each step)—evolve according to Eq. (16).<sup>63</sup> It is given by

$$\frac{dx_i(t)}{dt} = \sum_j \left[ \frac{\partial D_{ij}}{\partial x_j} - \beta D_{ij} \frac{\partial F}{\partial x_j} \right] + \sum_j g_{ij} \eta_j(t), \quad (20)$$

where  $\vec{x}(t)$  is the position of a random walker,  $D_{ij}$ ,  $F$ , and their derivatives are evaluated at  $\vec{x}(t)$ ,  $\eta$  is delta-correlated white noise with zero mean and unity variance (i.e.,  $\langle \eta_i \rangle = 0$ ,  $\langle \eta_i(t) \eta_j(t') \rangle = \delta(t - t') \delta_{ij}$ ), and  $\sum_k g_{ik} g_{kj} = 2D_{ij}$ .<sup>51</sup> The latter condition simplifies to  $g_{ij} = \sqrt{2D_i} \delta_{ij}$  if we assume the diffusion coefficient is diagonal and given by Eq. (7). Figure 16 shows an example of Langevin trajectory compared to a trajectory obtained by TPS, and Fig. 17 shows the probability distribution of finding a random walker as a function of time.

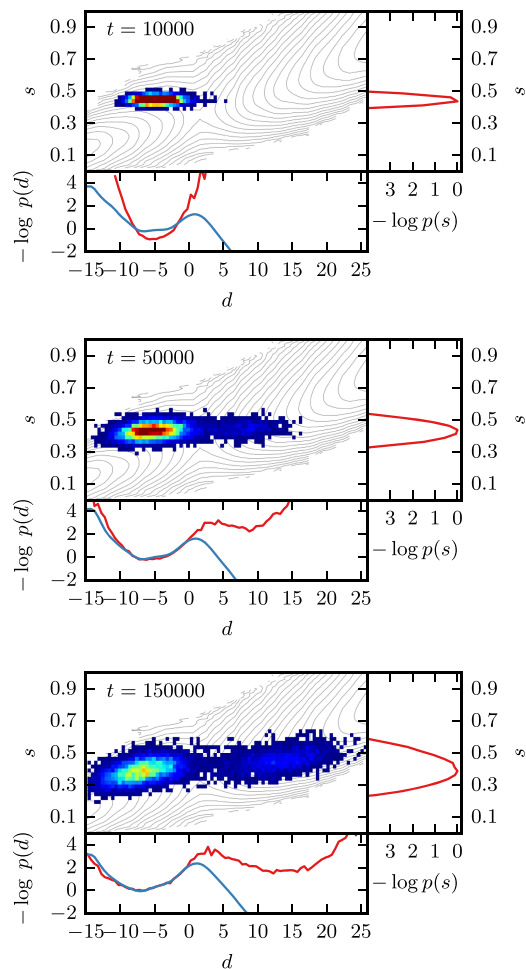


FIG. 17. Time evolution of the probability density function  $\rho(\vec{x}, t)$  as obtained by integrating trajectories using Eq. (20) and subsequently averaging over the positions  $x(t)$ . The random walkers are started at position  $d = -5$  and  $s = 0.45$ . Red indicates high densities and blue indicates low densities. In each of the plots, the bottom plot and the right plot show the negative logarithm of the probability density projected on each axis (red). In the bottom plot, the equilibrium free energy  $\beta F(d, s = \langle s \rangle_t)$  is shown (blue), where  $\langle s \rangle_t = \int dd \int ds s p(d, s; t)$  is the mean value of  $s$  at the given time.

These two diagrams demonstrate two things: first, the trajectories generated using a full simulation and the ones generated from the Langevin equation very much look alike, and, second, that indeed a relaxation towards equilibrium along the  $d$  coordinate occurs before the system has time to evolve to the stable basins.

## VI. DISCUSSION

We have investigated the disk-to-slab transition in the 2d-Ising model using a variety of methods, including a model based on a two-dimensional Smoluchowski equation. This model allows us to take the different time scales involved in this process into account: the fluctuations of the narrow bridge between the clusters (characterized by the  $d$ -coordinate) and the change of the overall shape of the cluster (captured by the  $s$ -coordinate). By comparing committor distributions obtained by brute-force using the full dynamics of the system, to the committor distribution obtained by solving the adjoint equation (17) (Fig. 15), we find that the dynamics of the transition are well described by the Smoluchowski equation (16).

This suggests that, with the coordinates  $d$  and  $s$ , we have indeed captured the degrees of freedom that are most relevant for the disk-to-slab transition. Increased values of  $s$ , corresponding to disk-like clusters, enhance the likelihood of a trajectory started from a configuration to develop towards the disk state. While stated in this way, this result does not seem surprising, it is nonetheless interesting to note, that this effect only becomes apparent when one includes the dynamics of the system into consideration, while the free energy landscape alone does not capture this feature.

In the disk-to-slab transition considered here, this behavior is caused by the large difference in time scales associated with the crossing of the free energy barrier and the relaxation towards the stable basins. As a consequence, a local quasi-equilibrium forms where the global shape of the cluster is fairly stable, while its surface fluctuates.

It is worth pointing out that this difference in time scales is due to the choice of dynamics that mimic local mass transport. A different choice of dynamics, for example, allowing the exchange of arbitrary spins or allowing the magnetization of the system to fluctuate,<sup>41</sup> will result in different behavior.

Our analysis highlights the fact that, even in the context of a fairly simple model system, the dynamics of a system are crucial to identifying transition mechanisms, especially when one needs to use a combination of multiple order parameters to obtain a good reaction coordinate. In particular, including dynamics may help to reconcile free energy landscapes and committor probabilities, or their combination may point to the existence of other important degrees of freedom.

## ACKNOWLEDGMENTS

The authors thank Georg Menzl and Phillip L. Geissler for many enlightening discussions. C.M. is supported by an uni:docs fellowship of the University of Vienna. A.T. acknowledges the support from the Austrian Science Fund (FWF)

Project No. P27738-N28. The computational results presented have been achieved in part using the Vienna Scientific Cluster (VSC).

## APPENDIX: MEAN FIRST PASSAGE TIME IN A LINEAR POTENTIAL

The estimate of the drift time in Eq. (14) is given by the mean first passage time (MFPT) in a potential with constant slope, i.e.,

$$\tilde{F}(s) = \left( \frac{\partial F(\tilde{s})}{\partial \tilde{s}} \right)_{\tilde{s}=s_0} (s - s_0), \quad (\text{A1})$$

where in the following we assume  $\partial F(s)/\partial s > 0$ .

Given the one-dimensional Fokker-Planck equation,

$$\frac{\partial \rho(s, t)}{\partial t} = -\frac{\partial}{\partial s} [A(s)\rho(s, t)] + \frac{1}{2} \frac{\partial^2}{\partial s^2} [B(s)\rho(s, t)], \quad (\text{A2})$$

the MFPT  $T(a; s_0)$  at an absorbing barrier  $a$  with a reflective barrier  $b$  located at  $b > a$  and given that trajectories are started at  $s_0$  is given by<sup>52</sup>

$$T(a; s_0) = 2 \int_a^{s_0} ds' \left[ \frac{1}{\psi(s')} \int_{s'}^b ds'' \frac{\psi(s'')}{B(s'')} \right], \quad (\text{A3})$$

with

$$\psi(s) = \exp \left[ \int_a^s ds' \frac{2A(s')}{B(s')} \right]. \quad (\text{A4})$$

Substituting  $A(s) = -\beta D_s (\partial F/\partial s)$  and  $B(s) = 2D_s$  with constant diffusion coefficient  $D_s$  and carrying out the integration yields

$$T(a; s_0) = \frac{e^{\beta g(a-b)} - e^{\beta g(s_0-b)} + \beta g(s_0 - a)}{D_s \beta^2 g^2}, \quad (\text{A5})$$

where  $g = \left( \frac{\partial F(s)}{\partial s} \right)_{s=s_0}$ . By setting  $a = s_0 - \Delta s$  and carrying out the limit  $b \rightarrow \infty$ , we arrive at the expression

$$T(s_0 - \Delta s; s_0) = \tau_{\text{drift}}(s_0) = \frac{\Delta s}{D_s \beta \left( \frac{\partial F(s)}{\partial s} \right)_{s=s_0}}. \quad (\text{A6})$$

<sup>1</sup>D. Frenkel, *Eur. Phys. J. Plus* **128**, 10 (2013).

<sup>2</sup>J. Chahine, R. J. Oliveira, V. B. P. Leite, and J. Wang, *Proc. Natl. Acad. Sci. U. S. A.* **104**, 14646 (2007).

<sup>3</sup>S. V. Krivov and M. Karplus, *Proc. Natl. Acad. Sci. U. S. A.* **105**, 13841 (2008).

<sup>4</sup>M. Hinczewski, Y. von Hansen, J. Dzubiella, and R. R. Netz, *J. Chem. Phys.* **132**, 245103 (2010).

<sup>5</sup>R. B. Best and G. Hummer, *Proc. Natl. Acad. Sci. U. S. A.* **107**, 1088 (2010).

<sup>6</sup>R. B. Best and G. Hummer, *Phys. Chem. Chem. Phys.* **13**, 16902 (2011).

<sup>7</sup>H. Trinkaus, *Phys. Rev. B* **27**, 7372 (1983).

<sup>8</sup>A. Berezhkovskii and A. Szabo, *J. Chem. Phys.* **122**, 014503 (2005).

<sup>9</sup>B. Peters, *J. Chem. Phys.* **131**, 244103 (2009).

<sup>10</sup>P. Tiwary and B. J. Berne, *J. Chem. Phys.* **147**, 152701 (2017).

<sup>11</sup>S. H. Northrup and J. A. McCammon, *J. Chem. Phys.* **78**, 987 (1983).

<sup>12</sup>G. J. Moro and F. Cardin, *Chem. Phys.* **235**, 189 (1998).

<sup>13</sup>L. Maragliano, A. Fischer, E. Vanden-Eijnden, and G. Ciccotti, *J. Chem. Phys.* **125**, 024106 (2006).

<sup>14</sup>S. Yang, J. N. Onuchic, A. E. García, and H. Levine, *J. Mol. Biol.* **372**, 756 (2007).

<sup>15</sup>E. Weinan and E. Vanden-Eijnden, *J. Stat. Phys.* **123**, 503 (2006).

<sup>16</sup>W. E, W. Ren, and E. Vanden-Eijnden, *Chem. Phys. Lett.* **413**, 242 (2005).

<sup>17</sup>P. Metzner, C. Schütte, and E. Vanden-Eijnden, *J. Chem. Phys.* **125**, 084110 (2006).

<sup>18</sup>K. Leung and R. K. P. Zia, *J. Phys. A: Math. Gen.* **23**, 4593 (1990).

<sup>19</sup>A. Tröster, C. Dellago, and W. Schranz, *Phys. Rev. B* **72**, 094103 (2005).

- <sup>20</sup>C. Singh, A. M. Jackson, F. Stellacci, and S. C. Glotzer, *J. Am. Chem. Soc.* **131**, 16377 (2009).
- <sup>21</sup>C. Singh, Y. Hu, B. P. Khanal, E. R. Zubarev, F. Stellacci, and S. C. Glotzer, *Nanoscale* **3**, 3244 (2011).
- <sup>22</sup>A. Santos, C. Singh, and S. C. Glotzer, *Phys. Rev. E* **81**, 011113 (2010).
- <sup>23</sup>V. Kumar, S. Sridhar, and J. R. Errington, *J. Chem. Phys.* **135**, 184702 (2011).
- <sup>24</sup>S. Prestipino, C. Caccamo, D. Costa, G. Malescio, and G. Munaò, *Phys. Rev. E* **92**, 022141 (2015).
- <sup>25</sup>K. Lum and D. Chandler, *Int. J. Thermophys.* **19**, 845 (1998).
- <sup>26</sup>D. Nicolaides and R. Evans, *Phys. Rev. B* **39**, 9336 (1989).
- <sup>27</sup>R. Evans, *J. Phys.: Condens. Matter* **2**, 8989 (1999).
- <sup>28</sup>P. G. Bolhuis and D. Chandler, *J. Chem. Phys.* **113**, 8154 (2000).
- <sup>29</sup>K. Leung and A. Luzar, *J. Chem. Phys.* **113**, 5845 (2000).
- <sup>30</sup>A. Luzar and K. Leung, *J. Chem. Phys.* **113**, 5836 (2000).
- <sup>31</sup>A. Vishnyakov and A. V. Neimark, *J. Chem. Phys.* **119**, 9755 (2003).
- <sup>32</sup>R. C. Remsing, E. Xi, S. Vembanur, S. Sharma, P. G. Debenedetti, S. Garde, and A. J. Patel, *Proc. Natl. Acad. Sci. U. S. A.* **112**, 8181 (2015).
- <sup>33</sup>J. Plateau, *Statique des Liquides Soumis aux Seuls Forces Moléculaires* (Gauthier-Villars, Paris, 1873), Vol. 2.
- <sup>34</sup>Lord Rayleigh, *Proc. London Math. S.* **s1-10**, 4 (1878).
- <sup>35</sup>S. A. Safran, *Statistical Thermodynamics of Surfaces, Interfaces, and Membranes* (Westview Press, 2003).
- <sup>36</sup>A. Tröster and K. Binder, *Phys. Rev. Lett.* **107**, 265701 (2011).
- <sup>37</sup>A. Tröster, M. Oettel, B. Block, P. Virnau, and K. Binder, *J. Chem. Phys.* **136**, 064709 (2012).
- <sup>38</sup>T. Neuhaus and J. S. Hager, *J. Stat. Phys.* **113**, 47 (2003).
- <sup>39</sup>S. Trebst, D. A. Huse, and M. Troyer, *Phys. Rev. E* **70**, 046701 (2004).
- <sup>40</sup>W. E and E. Vanden-Eijnden, *Annu. Rev. Phys. Chem.* **61**, 391 (2010).
- <sup>41</sup>M. Venturoli, E. Vanden-Eijnden, and G. Ciccotti, *J. Math. Chem.* **45**, 188 (2009).
- <sup>42</sup>K. Kawasaki, *Phys. Rev.* **145**, 224 (1966).
- <sup>43</sup>F. Schmitz, P. Virnau, and K. Binder, *Phys. Rev. E* **87**, 053302 (2013).
- <sup>44</sup>K. Binder and P. Virnau, *J. Chem. Phys.* **145**, 211701 (2016).
- <sup>45</sup>P. L. Geissler, C. Dellago, and D. Chandler, *Phys. Chem. Chem. Phys.* **1**, 1317 (1999).
- <sup>46</sup>A. Ferrenberg and R. Swendsen, *Phys. Rev. Lett.* **63**, 1195 (1989).
- <sup>47</sup>S. Kumar, J. M. Rosenberg, D. Bouzida, R. H. Swendsen, and P. A. Kollman, *J. Comput. Chem.* **13**, 1011 (1992).
- <sup>48</sup>A. Grossfield, *WHAM: The Weighted Histogram Analysis Method* (2013), <http://membrane.urmc.rochester.edu/content/wham>.
- <sup>49</sup>B. Peters and B. L. Trout, *J. Chem. Phys.* **125**, 054108 (2006).
- <sup>50</sup>C. Dellago, P. G. Bolhuis, and P. L. Geissler, *Adv. Chem. Phys.* **123**, 1–78 (2002).
- <sup>51</sup>H. Risken, *The Fokker-Planck Equation: Methods of Solution and Applications* (Springer, Berlin, Heidelberg, 1984).
- <sup>52</sup>C. W. Gardiner *et al.*, *Handbook of Stochastic Methods* (Springer, Berlin, 1985), Vol. 3.
- <sup>53</sup>W. Im and B. Roux, *J. Mol. Biol.* **319**, 1177 (2002).
- <sup>54</sup>A. C. Pan, D. Sezer, and B. Roux, *J. Phys. Chem. B* **112**, 3432 (2008).
- <sup>55</sup>G. Hummer, *New J. Phys.* **7**, 34 (2005).
- <sup>56</sup>D. J. Bicout and A. Szabo, *J. Chem. Phys.* **109**, 2325 (1998).
- <sup>57</sup>A. H. Al-Mohy and N. J. Higham, *SIAM J. Matrix Anal. Appl.* **31**, 970 (2010).
- <sup>58</sup>E. Jones, T. Oliphant, P. Peterson *et al.*, SciPy: Open source scientific tools for Python, <http://www.scipy.org/>.
- <sup>59</sup>H. Kramers, *Physica* **7**, 284 (1940).
- <sup>60</sup>K. Schulten, Z. Schulten, and A. Szabo, *J. Chem. Phys.* **74**, 4426 (1981).
- <sup>61</sup>Note that in slices with higher free energy barriers, we are likely to underestimate  $\tau_{\text{cross}}$  since  $1/[\Delta d]^2$  will be smaller than the product of curvatures used in Kramers' theory.
- <sup>62</sup>The Smoluchowski equation (16) is often rewritten in the form  $\frac{\partial \rho}{\partial t} = \sum_i \frac{\partial}{\partial x_i} \left[ \sum_j D_{ij} e^{-\beta F} \frac{\partial}{\partial x_j} (e^{\beta F} \rho) \right]$  that makes it immediately obvious that the equilibrium distribution is the stationary solution.
- <sup>63</sup>P. F. Tupper and X. Yang, *Proc. R. Soc. A* **468**, 3864 (2012).